Progress In Electromagnetics Research C, Vol. 172, 89–102, 2026

PIER C

(Received 4 June 2026, Accepted 6 July 2026, Scheduled 1 August 2026)

# Open-Circuit Fault Diagnosis of Quasi-Z-Source Inverter Systems Based on IST-NFTSMO and ALLR-SCR Hybrid Features

Yang Zhang*, Moutao Li, Shaoziyi Wu, Jiahao Zhang, and Qianghui Xiao

*Hunan University of Technology, Zhuzhou, 412007, China*

**ABSTRACT:** The open-circuit fault diagnosis of switches in quasi-Z-source inverters (qZSI) is challenging. Existing methods struggle to simultaneously achieve high robustness and low computational complexity without additional sensors. In this study, an open-circuit fault diagnosis method based on an improved super-twisting non-singular fast terminal sliding-mode observer (IST-NFTSMO) and hybrid features is proposed. The stator currents were estimated in real time by the IST-NFTSMO, and residuals were generated accordingly. By analyzing differences in the statistical distributions of residuals between healthy and faulty conditions, two features were extracted: average log-likelihood ratio (ALLR) and signed cumulative ratio (SCR). The ALLR is used for rapid fault detection, whereas the SCR is used for accurate localization of faulty switches. The proposed method was implemented entirely based on existing current sensors. No additional voltage sensors were required. Moreover, the diagnostic thresholds are adaptively adjusted according to variations in speed and load. The experimental results demonstrate that both single-switch and dual-switch open-circuit faults can be diagnosed rapidly and accurately. Compared with conventional methods, higher robustness and lower computational complexity were achieved.

## 1. INTRODUCTION

Permanent magnet synchronous motors (PMSMs) have been widely adopted in high-performance drive applications, including industrial servo systems, rail transit, and electric vehicles, owing to their high efficiency, torque density, and excellent dynamic performance [1–3]. With the rapid development of power electronics technology, significant improvements have been achieved in the control precision and efficiency of PMSM drive systems. Among the various inverter topologies, the quasi-Z-source inverter (qZSI) has attracted considerable research interest in the fields of renewable energy grid integration and motor drives [4–7]. This is attributed to its unique impedance network structure, which enables buck-boost conversion within a single-stage circuit and permits the shoot-through state of the inverter bridge. Consequently, the adaptability of the system to input voltage fluctuations was substantially enhanced. However, most existing open-circuit fault diagnosis methods for qZSI systems rely on additional voltage sensors or large volumes of training data [8]. Moreover, the diagnostic thresholds are typically fixed, making it difficult to accommodate wide variations in the speed and load. In addition, existing methods generally focus on fault features derived from voltage residuals [9], specific topologies [10, 11], and current errors [12]. The statistical distribution characteristics of the observer residuals have not been sufficiently exploited. Consequently, the diagnostic robustness is limited under noisy and transient operating conditions. Therefore, the development of a novel diagnostic method that eliminates the need for additional sensors, fully exploits residual statistical features, and enables adaptive threshold adjustment is urgently needed.

Currently, research on open-circuit faults of switching devices in QZ-source inverters remains limited. Existing diagnosis methods for inverter open-circuit faults can be mainly categorized into three types: voltage-signal-based, current-signal-based, and data-driven methods. Voltage-based methods achieve fault diagnosis using terminal voltages or voltage residuals [13]. A faster response is offered. However, additional voltage sensors and acquisition circuits are required, which increases system cost and complexity. Current-based methods utilize features such as current vector trajectories and average current Park vectors [14, 15]. No additional sensors were required. Nevertheless, heavy computational burden and insufficient robustness are exhibited under dynamic operating conditions. Data-driven methods, such as deep neural networks (DNNs), can avoid physical modeling. However, their diagnostic reliability is highly dependent on large volumes of training data, and their generalization capability is difficult to guarantee [16]. More importantly, none of the above methods fully exploit the dynamic response characteristics of the qZS impedance network under fault conditions. The diagnostic thresholds are typically fixed, making it difficult to maintain satisfactory performance under wide variations in the speed and load. Additional methods include the average current Park vector method [17], normalized DC method [18], improved normalized DC method [19], load current analysis method [20], and simple DC method [21]. In [22], a current vector trajectory centroid method was proposed. The fault features were compressed through the centroid, and the traditional trajectory-shape-based analysis was simplified. However, system symmetry is required, and the dynamic robustness is insufficient. For voltage-signal-based methods, the main approaches include the analytical model method, lower-arm voltage detec-

* Corresponding author: Yang Zhang(459387623@qq.com).

tion method, voltage residual method, and switching function model. In studies on different voltage residual methods, the diagnostic features can be classified as follows: phase voltage residuals [23], line voltage residuals [24], pole voltage residuals [25], and neutral point voltage residuals [26]. In these methods, voltage residuals are calculated by comparing the output voltage with the reference voltage using various processing techniques, and fault diagnosis is then performed. Although the diagnostic time can be shortened by using voltage features, additional measurement devices, such as voltage sensors and voltage acquisition circuits, are required, which increases detection cost.

To overcome the aforementioned limitations, an open-circuit fault diagnosis method for qZSI-PMSM drives is proposed in this study within the framework of modulated predictive power control (MPPC). The main contributions of this study are summarized as follows.

(1) A current residual generation method based on an improved super-twisting non-singular fast terminal sliding mode observer (IST-NFTSMO) is proposed. In the designed observer, a closed-loop feedback term was introduced to accelerate the convergence of the sliding surface. The rapid tracking of system states under abrupt lumped disturbances caused by open-circuit faults was achieved. Consequently, the high sensitivity of the current residual to faults is ensured.

(2) A hybrid fault feature extraction strategy based on the average log-likelihood ratio (ALLR) and signed cumulative ratio (SCR) is proposed. By exploiting the differences in statistical distributions of current residuals before and after faults, ALLR is employed for rapid fault detection, whereas SCR is employed for precise fault localization. The decoupling between detection and localization is realized. The trade-off between the diagnostic speed and localization accuracy inherent in single-feature methods is avoided.

(3) A delayed-switching adaptive threshold mechanism is designed. Under normal operating conditions, the threshold is determined based on the interquartile range (IQR) of historical residual data. After a fault occurs, the faulty phase is excluded from the threshold update queue using a delayed signal. The threshold adjustment is driven solely by healthy-phase data. The contamination of the threshold by fault data was effectively prevented. Robustness of the diagnosis under varying operating conditions is guaranteed.

(4) The proposed method relies entirely on the existing current sensors in the system. No additional voltage sensors or large-scale training data are required for this method. The diagnosis of single-switch and various types of double-switch open-circuit faults can be achieved within a unified framework. The proposed method demonstrates low computational complexity and good engineering practicality.

The effectiveness and practicality of the proposed method were fully validated through detailed RT-LAB hardware-in-the-loop experiments under single-switch and double-switch open-circuit fault conditions. The remainder of this study is organized as follows. In Section 2, the mathematical model of the qZSI-PMSM system is established, and current path variations and fault characteristics under open-circuit faults are analyzed. In Section 3, the IST-NFTSMO observer is designed, the generation method of the current residuals is derived, and the fault-sensitive characteristics are analyzed. In Section 4, the fault detection and localization strategy based on ALLR-SCR hybrid features is elaborated in detail, and the design method of the delayed-switching adaptive threshold is presented. In Section 5, the effectiveness of the proposed method is verified using RT-LAB hardware-in-the-loop experiments. Section 6 provides conclusions of the study.

## 2. MODELING OF THE QUASI-Z-SOURCE INVERTER-PMSM SYSTEM

### 2.1. Topology and Operating Modes of the Quasi-Z-Source Inverter

The qZSI is a single-stage buck-boost inverter that offers a continuous input current, reduced capacitor voltage stress, and inherent tolerance of the shoot-through state. It operates in two distinct modes:

In the non-shoot-through (NST) mode, the inverter bridge switches in a normal manner to supply an AC voltage to the load. Diode $D$ conducts, and energy is delivered to the load via the inverter bridge, while inductors $L_1$ and $L_2$ release stored energy and, together with the input source, charge capacitors $C_1$ and $C_2$.

In the shoot-through (ST) mode, the upper and lower switches of one inverter leg conduct simultaneously, thereby creating a short circuit. During this interval, inductors $L_1$ and $L_2$ store energy, and capacitors $C_1$ and $C_2$ discharge. The output voltage is controlled by adjusting the ST duty ratio $d$ and NST duty ratio $(1-d)$.

Figure 3 shows the topology of the qZSI-PMSM system. The QZ-source network comprises two identical inductors ($L_1 = L_2$), two identical capacitors ($C_1 = C_2$), a single diode, and a DC power supply. These components primarily perform energy storage and boost the voltage.

Under open-circuit fault conditions, the normal current path is disrupted. Fig. 1 illustrates the current path when a single-switch open-circuit fault occurs. Various types of double-switch faults, such as cross-side, same-side, and single-phase open-circuit faults, are depicted in Fig. 2.

### 2.2. Mixed Logical Dynamic Model and State-Space Averaging

Because the qZSI contains power-switching devices, its mathematical model is inherently a hybrid system that couples continuous dynamic behavior with discrete switching events, thus exhibiting nonlinear switching characteristics.

To construct the state-space representation, the circuit operation of the QZ-source network in both the NST and ST modes is first analyzed using Kirchhoff's voltage and current laws (KVL and KCL). This analysis accounts for the dynamic behavior of inductors and capacitors, as well as the switching circuit modes. The inductor currents and capacitor voltages are chosen as the state variables, and the state equations for the NST mode are as follows:

$$\begin{cases} L_1 \dfrac{di_{L1}}{dt} = u_{in} - u_{C1} \\ L_2 \dfrac{di_{L2}}{dt} = -u_{C2} \\ C_1 \dfrac{dv_{C1}}{dt} = i_{L2} - i_{PN} \\ C_2 \dfrac{dv_{C2}}{dt} = i_{L1} - i_{PN} \end{cases} \tag{1}$$

The state equations under the ST mode are expressed as:

$$\begin{cases} L_1 \dfrac{di_{L1}}{dt} = u_{in} + u_{C2} \\ L_2 \dfrac{di_{L2}}{dt} = u_{C1} \\ C_1 \dfrac{dv_{C1}}{dt} = -i_{L2} \\ C_2 \dfrac{dv_{C2}}{dt} = -i_{L1} \end{cases} \tag{2}$$

In (1) and (2), $i_{L1}$ and $i_{L2}$ denote the currents of inductors $L_1$ and $L_2$; $u_{C1}$ and $u_{C2}$ denote the voltages of capacitors $C_1$ and $C_2$; $u_{in}$ is the input voltage of the qZSI; and $i_{PN}$ is the input current of the inverter.

The state-space averaging method is employed to capture the dynamic behavior over an entire switching cycle. The equations corresponding to both operating modes are combined through weighted averaging, using the fixed ST duty ratio $d$ and NST duty ratio $(1-d)$. This yields the averaged state equation:

$$\dot{X} = (1-d)\dot{X}_{\text{NST}} + d\dot{X}_{\text{ST}} \tag{3}$$

where $X_{\text{NST}}$ and $X_{\text{ST}}$ are the state vectors in the NST and ST modes, respectively. The average state equation is derived as follows:

$$\begin{cases} L_1 \dfrac{di_{L1}}{dt} = u_{in} - (1-d)u_{C1} + du_{C2} \\ L_2 \dfrac{di_{L2}}{dt} = -(1-d)u_{C2} + du_{C1} \\ C_1 \dfrac{dv_{C1}}{dt} = -(1-d)(i_{L2} + i_{PN}) \\ C_2 \dfrac{dv_{C2}}{dt} = (1-d)(i_{L1} - i_{PN}) - di_{L2} \end{cases} \tag{4}$$

This model is nonlinear because a product relationship exists between the state variables and the duty ratio $d$. Therefore, a stable operating point $(i_{L1}, i_{L2}, u_{C1}, u_{C2})$ is selected, and small perturbations $(\Delta i_{L1}, \Delta i_{L2}, \Delta u_{C1}, \Delta u_{C2})$ are introduced. Through Taylor expansion with higher-order terms neglected, the linearized state-space model is obtained as:

$$\begin{bmatrix} L_1 \dfrac{d\Delta i_{L1}}{dt} \\ L_2 \dfrac{d\Delta i_{L2}}{dt} \\ C_1 \dfrac{d\Delta u_{C1}}{dt} \\ C_2 \dfrac{d\Delta u_{C2}}{dt} \end{bmatrix} = A \begin{bmatrix} i_{L1} \\ i_{L2} \\ u_{C1} \\ u_{C2} \end{bmatrix} + B \begin{bmatrix} u_{in} \\ i_{PN} \end{bmatrix} \tag{5}$$

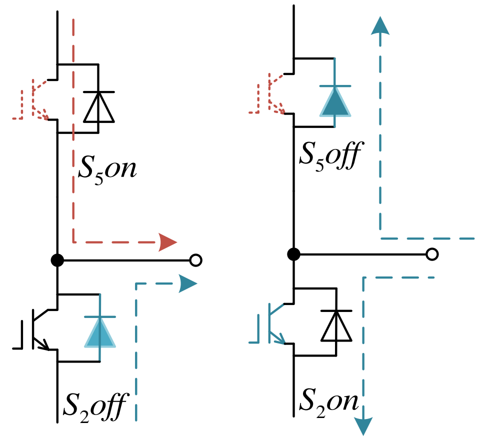


**FIGURE 1**. Current path under single-switch fault.

where:

$$\mathbf{A} = \begin{bmatrix} 0 & 0 & -(1-d)/L_1 & d/L_1 \\ 0 & 0 & d/L2 & -(1-d)/L_2 \\ 0 & -(1-d)/C_1 & 0 & 0 \\ (1-d)/C_2 & -d/C_2 & 0 & 0 \end{bmatrix} \tag{6}$$

$$\mathbf{B} = \begin{bmatrix} 1/L_1 & 0 \\ 0 & 0 \\ 0 & -(1-d)/C_1 \\ 0 & -(1-d)/C_2 \end{bmatrix} \tag{7}$$

**A** is the system matrix that represents the dynamic relationships among the state variables. **B** is the input matrix, which represents the effects of the control input variables $u_{in}$ and $i_{PN}$ on the state variables.

### 2.3. Mathematical Model of PMSM

A surface-mounted permanent magnet synchronous motor (SPMSM) was adopted in the drive system of this study. A sinusoidal air-gap magnetic-field distribution was assumed. The core saturation and eddy current losses were neglected. In the rotor synchronous rotating reference frame, the stator voltage equation is expressed as:

$$\begin{cases} u_d = R_s i_d + L \dfrac{di_d}{dt} - \omega_e L i_q \\ u_q = R_s i_q + L \dfrac{di_q}{dt} + \omega_e (L i_d + \psi_f) \end{cases} \tag{8}$$

where $u_d$ and $u_q$ are the $d$-axis and $q$-axis stator voltages, respectively; $i_d$ and $i_q$ are the $d$-axis and $q$-axis stator currents, respectively; $R_s$ and $L_s$ are the stator resistance and inductance, respectively, with $L_d = L_q = L_s$ in the SPMSM; $\omega_e$ is the electrical angular speed; and $\psi_f$ is the permanent magnet flux linkage.

By rearranging (8) into the form with currents as state variables, the following equation is obtained:

$$\begin{cases} \dfrac{di_d}{dt} = -\dfrac{R_s}{L} i_d + \omega_e i_q + \dfrac{1}{L} u_d \\ \dfrac{di_q}{dt} = -\dfrac{R_s}{L} i_q - \omega_e i_d - \dfrac{\omega_e \psi_f}{L} + \dfrac{1}{L} u_q \end{cases} \tag{9}$$

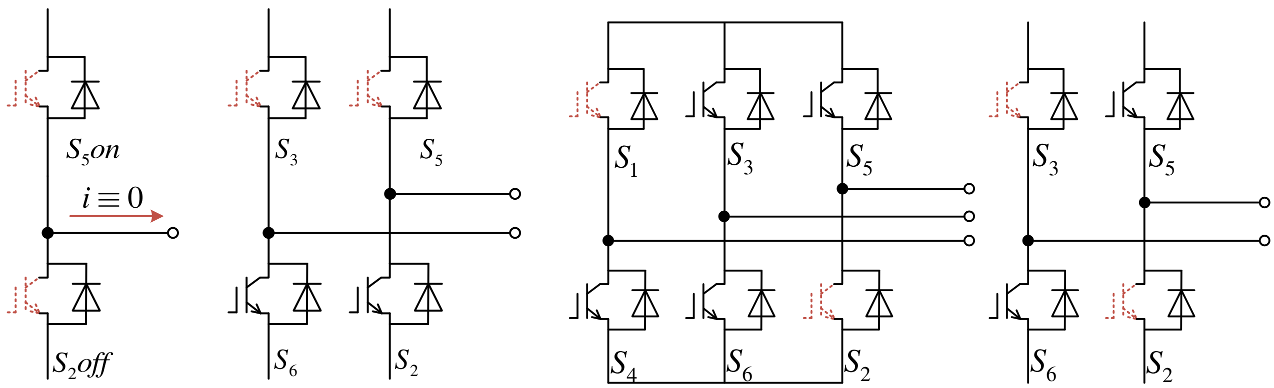


**FIGURE 2**. Cross-side dual-switch open-circuit fault, same-side dual-switch open-circuit fault, and single-phase dual-switch open-circuit fault.

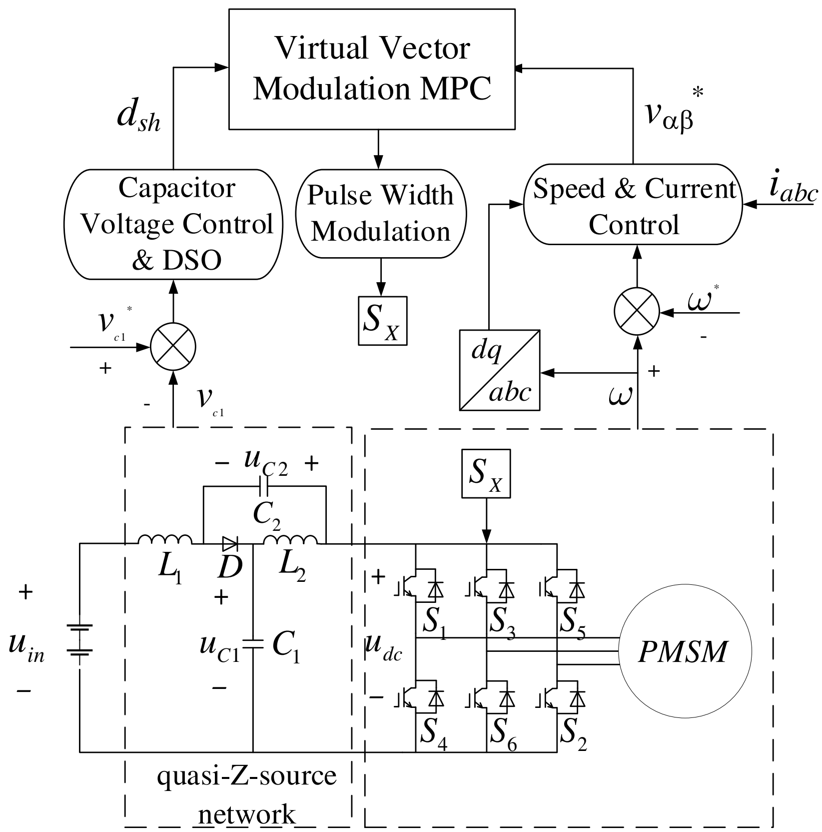


**FIGURE 3**. Topology and control methods of qZSI.

By defining the state vector $\mathbf{x} = [i_d, i_q]^T$ and the input vector $\mathbf{u} = [u_d, u_q]^T$, (9) can be written in matrix form as:

$$\frac{di}{dt} = \mathbf{A}\ \mathbf{i} + \mathbf{B}\ \mathbf{u} + \mathbf{d} \tag{10}$$

In (10), $\mathbf{d}(t)$ represents the lumped disturbance of the system under nominal operating conditions. It explicitly originates from the back-EMF dynamics produced by the coupling of the permanent magnet flux linkage and rotational speed. When the system operates under healthy conditions, this disturbance vector is the only non-zero deterministic component. Once an open-circuit fault occurs in the inverter, the actual terminal voltage fed to the motor deviates from the reference voltage specified by the controller. This variation can be equivalently treated as an unknown fault vector that is superimposed on the input channel. Consequently, the lumped disturbance of the system is expanded to $\mathbf{d}(t) + \Delta\mathbf{d}_f(t)$, where the additional term $\Delta\mathbf{d}_f(t)$ contains all abnormal current dynamic information caused by the fault.

## 3. CURRENT ESTIMATION AND RESIDUAL GENERATION BASED ON IST-NFTSMO

The observer design is premised on a clear understanding of the disturbance structure of the controlled plant. As can be seen from the state-space averaging model in Section 2.2, the actual output voltage of the qZSI inverter bridge is jointly affected by the switching transient of the shoot-through duty ratio, state ripple of the impedance network, and dead-time effect of the power devices during operation. A bounded deviation always exists between the actual output voltage and the ideal reference voltage provided by the controller, that is:

$$u_{abc} = u_{abc}^{ref} + \Delta u_{qZS} \quad \|\Delta u_{qZS}\| \leq \delta_{qZS} \tag{11}$$

where the upper bound is jointly determined by the qZS network parameters and DC bus voltage. It can be estimated offline based on the linearized model presented in Section 2.2. On this basis, when the current observer is constructed in this study, the voltage deviation and back-EMF dynamics of the PMSM are unified and incorporated into the lumped disturbance vector $d(t)$:

$$d(t) = d_E(t) + B^{-1}\Delta u_{qZS}(t) \tag{12}$$

where de$(t)$ is the back-EMF component produced by the coupling of permanent magnet flux linkage and rotational speed, and $B$ is the input matrix. Under this lumped-disturbance framework, explicit modeling and state reconstruction of the qZSI internal dynamics are not required by the observer. Instead, the robust compensation capability of the super-twisting control law in the IST-NFTSMO against bounded matched disturbances is utilized. The influence on the current estimation accuracy is automatically suppressed during the sliding mode reaching phase. Consequently, the current residual is maintained with approximately zero-mean narrow-band distribution characteristics under normal operating conditions.

### 3.1. Stator Current State Equation and Observer Structure Design

The PMSM state equation with stator currents as state variables is expressed as:

$$\dot{\mathbf{x}} = \mathbf{A}\mathbf{x} + \mathbf{B}\mathbf{u} + \mathbf{D}\mathbf{f} \tag{13}$$

where $\mathbf{x} = [i_d, i_q]^T$, $\mathbf{A}_0 = \mathbf{A} - \mathbf{B}R_s/L_s$, $\mathbf{d}(t)$ is the lumped disturbance vector, and $\mathbf{A}$ is the coefficient matrix, with:

$$\mathbf{A} = \begin{bmatrix} -\dfrac{R_s}{L} & \omega_e \\ -\omega_e & -\dfrac{R_s}{L} \end{bmatrix}, \quad \mathbf{B} = \begin{bmatrix} \dfrac{1}{L} & 0 \\ 0 & \dfrac{1}{L} \end{bmatrix}, \quad \mathbf{D} = \begin{bmatrix} 0 & \dfrac{1}{L} \\ \dfrac{1}{L} & 0 \end{bmatrix}.$$

Based on (13), the IST-NFTSMO is designed as follows:

$$\dot{\hat{\mathbf{x}}} = \mathbf{A}\hat{\mathbf{x}} + \mathbf{B}\mathbf{u} + \mathbf{v} \tag{14}$$

where $\hat{\mathbf{x}}$ is the estimated value of $\mathbf{x}$, and $\mathbf{v}$ is the sliding mode control term.

It is worth noting that parameter uncertainties, such as variations in stator resistance $R_s$ and inductance $L_s$ due to temperature or saturation effects, can be treated as additional matched disturbances. These uncertainties are bounded in practice and can be incorporated into the lumped disturbance term $\mathbf{d}(t)$. Consequently, the boundedness assumption $\|\mathbf{d}(t)\| \leq D_1$ and $\|\dot{\mathbf{d}}(t)\| \leq D_2$ remains valid with slightly enlarged constants $D_1, D_2$ that cover the worst-case parameter drift.

By subtracting (14) from (13), the current error state equation is obtained as:

$$\dot{\mathbf{e}} = \mathbf{A}\mathbf{e} + \mathbf{D}\mathbf{f} - \mathbf{v} \tag{15}$$

where $\mathbf{e} = \mathbf{x} - \hat{\mathbf{x}}$ is the current estimation error, and $\bar{\mathbf{d}}(t) = \mathbf{d}(t) - \hat{\mathbf{d}}(t)$.

To improve the convergence speed of the current error, a non-singular fast terminal sliding surface is designed as:

$$s_n = \alpha\mathbf{e} + \beta\mathbf{e}^{m/r} + \lambda\dot{\mathbf{e}} + \mu\dot{\mathbf{e}}^{p/q} \tag{16}$$

where $\alpha = \mathrm{diag}(\alpha_1, \alpha_2)$, $\beta = \mathrm{diag}(\beta_1, \beta_2)$, $\gamma = \mathrm{diag}(\gamma_1, \gamma_2)$, and $\lambda = \mathrm{diag}(\lambda_1, \lambda_2)$ are positive parameter matrices to be designed; $m$, $r$, $p$, and $q$ are odd constants to be designed, satisfying $m > r$, $p > q$, and $r/m < p/q$.

By taking the derivative of (17), the following is obtained:

$$\dot{s}_n = \alpha\dot{\mathbf{e}} + \frac{m}{r}\beta\mathbf{e}^{m/r-1}\dot{\mathbf{e}} + \lambda\ddot{\mathbf{e}} + \frac{p}{q}\mu\dot{\mathbf{e}}^{p/q-1}\ddot{\mathbf{e}} \tag{17}$$

To increase the speed at which the system state variables reach the sliding surface, an improved super-twisting control law is introduced as follows:

$$\begin{cases} \dot{s}_n = \displaystyle\int_0^t \begin{bmatrix} \frac{\alpha\dot{e} + \frac{m}{r}\beta e^{m/r-1}\dot{e}}{\lambda + \frac{p}{q}\mu|\dot{e}|^{p/q-1}} + k_1|s_n|^{0.5}\mathrm{sgn}(s_n) \\ +k_2 s_n - \sigma \end{bmatrix} d\tau \\ \dot{\sigma} = -k_3\mathrm{sgn}(s_n) - k_4\sigma \end{cases} \tag{18}$$

where $k_1, k_2, k_3$, and $k_4$ are positive parameter matrices to be designed, with $k_1 = \mathrm{diag}(k_{11}, k_{12})$, $k_2 = \mathrm{diag}(k_{21}, k_{22})$, $k_3 = \mathrm{diag}(k_{31}, k_{32})$, and $k_4 = \mathrm{diag}(k_{41}, k_{42})$; sgn$(\cdot)$ is the sign function; and **z** is an auxiliary variable.

An improved super-twisting control law is developed by introducing a closed-loop feedback term into the conventional super-twisting algorithm. The feedback of the auxiliary variable is used to improve the dynamic response, and the system state variables are driven to reach the sliding surface more rapidly than the conventional method. Meanwhile, the dynamic coupling relationship between $s$ and $\dot{s}$ is not altered, so that the fundamental regulation performance of the conventional super-twisting algorithm is preserved.

**Theorem 1:** Consider the error dynamics (15) under the bounded disturbance assumption $\|\mathbf{d}(t)\| \leq D_1$, $\|\dot{\mathbf{d}}(t)\| \leq D_2$. Select the non-singular fast terminal sliding surface as (16) and the improved super-twisting control law as (18). If the observer gains are chosen for each dimension $i = d, q$ as $k_{1i} > 2\sqrt{k_{3i}}$, $k_{3i} > D_{2i}$, $k_{2i}, k_{4i} > 0$, then the sliding variable **s** converges to zero in finite time, and the estimation error **e** converges to zero in finite time.

$$\begin{cases} \mathbf{v} = \mathbf{v}_{eq} + \mathbf{v}_n \\ \mathbf{v}_{eq} = \mathbf{A}\mathbf{e} \\ \mathbf{v}_n = \displaystyle\int_0^t \begin{bmatrix} \frac{\alpha\dot{e} + \frac{m}{r}\beta e^{m/r-1}\dot{e}}{\frac{p}{q}\mu\dot{\mathbf{e}}^{p/q-1} + \lambda} + k_1|s_n|^{0.5}\mathrm{sgn}(s_n) \\ +k_2 s_n - \sigma \end{bmatrix} d\tau \\ \dot{\sigma} = -k_3\mathrm{sgn}(s_n) - k_4\sigma \end{cases} \tag{19}$$

**Proof:** A Lyapunov function $V_1$ is selected as:

$$V_1 = s_n^T s_n \tag{20}$$

By taking the derivative of (20), the following is obtained:

$$\dot{V}_1 = 2s_n^T\dot{s}_n \tag{21}$$

By taking the derivative of (15), the following is obtained:

$$\dot{\mathbf{e}} = \mathbf{A}\dot{\mathbf{e}} + \mathbf{D}\dot{\mathbf{d}} - \dot{\mathbf{v}} \tag{22}$$

By substituting (22) into (21), the following is obtained:

$$\dot{V}_1 = 2s_n^T \begin{bmatrix} \left(\alpha + \frac{m}{r}\beta e^{m/r-1}\right)\dot{\mathbf{e}} + \lambda(\mathbf{A}\dot{\mathbf{e}} + \mathbf{D}\dot{\mathbf{d}} - \dot{\mathbf{v}}) \\ +\frac{p}{q}\mu e^{p/q-1}\left(A\dot{e} + D\dot{d} - \dot{v}\right) \end{bmatrix} \tag{23}$$

By taking the derivative of (19), the following is obtained:

$$\dot{\mathbf{v}} = \mathbf{A}\dot{\mathbf{e}} + \frac{\alpha\dot{e} + \frac{m}{r}\beta e^{m/r-1}\dot{e}}{\lambda + \frac{p}{q}\mu\dot{e}^{p/q-1}} + k_2 s_n - \sigma$$
$$+k_1|s_n|^{0.5}\text{sgn}(s_n) \tag{24}$$

By substituting (24) into (23), the following is obtained:

$$\dot{V}_1 = 2s_n^T\left(\lambda + \frac{p}{q}\mu\dot{e}^{p/q-1}\right)$$
$$\left[D\dot{f} - k_1|s_n|^{0.5}\text{sgn}(s_n) - k_2 s_n + \sigma\right] \tag{25}$$

Equation (25) can also be expressed as:

$$\dot{V}_1 = 2\sum_{i=1}^{2} s_{n,i}\left(\lambda + \frac{p}{q}\mu|\dot{e}|^{p/q-1}\right)$$
$$\left(D_i\dot{f}_i - k_1|s_{n,i}|^{0.5}\text{sgn}(s_{n,i}) - k_2 s_{n,i} + \sigma_i\right) \tag{26}$$

### 3.2. Improved Super-Twisting Control Law and Stability Proof

An improved super-twisting control law was designed based on the conventional super-twisting algorithm. A closed-loop feedback term is introduced through auxiliary variable **z** to improve the dynamic response. Thus, the system state variables are driven to reach the sliding surface more rapidly. Meanwhile, the dynamic coupling relationship between **s** and $\dot{\mathbf{s}}$ is not altered, so that the fundamental regulation performance of the conventional super-twisting algorithm is preserved.

Under open-circuit faults of the qZSI-SPMSM system, the lumped disturbance and its derivative are assumed to be bounded. That is, positive constants $D_1$ and $D_2$ exist such that $\|\tilde{\mathbf{d}}(t)\| \leq D_1$ and $\|\dot{\tilde{\mathbf{d}}}(t)\| \leq D_2$.

Furthermore, in (26), the terms $k_3\gamma\text{sgn}(s)$, $k_4\beta\text{sgn}(\dot{s})$, $k_1$ and $k_2$ act in directions opposite to $s$ and $\dot{s}$, thereby contributing negative-definite components to $\dot{V}_1$. Based on this property, the following inequality is derived from (25):

$$\dot{V}_1 \leq -2\min\left(\lambda + \frac{p}{q}\mu\dot{e}^{p/q-1}\right)\left(k_1\|s_n\|_1 + k_2\|s_n\|^2\right)$$
$$+2\|D\|F\|s_n\| \tag{27}$$

By appropriately increasing the control gain parameters, the condition $\dot{V}_1 < 0$ can be guaranteed. Thus:

$$\dot{V}_1 \leq -\eta\sqrt{V_1}, \quad \eta > 0 \tag{28}$$

Inequality (28) implies $\dot{V}_1 \leq -\eta\sqrt{V_1}$ for some $\eta > 0$ when the gain conditions above are satisfied. Hence $V_1(t)$ reaches zero within a finite time $t_f \leq 2\sqrt{V_1(0)}/\eta 9$, guaranteeing that $s \to 0$ and $\dot{s} \to 0$ in finite time. Once $s \equiv 0$, the structure of the NFTSM surface (16) drives the estimation error **e** to zero in finite time. Therefore, the overall observer convergence is finite-time and robust against both external disturbances and internal parameter uncertainties.

### 3.3. Generation of Current Residual and Fault-Sensitive Characteristic Analysis

The current estimation residual is defined as:

$$\mathbf{r}(t) = \mathbf{i}_s(t) - \hat{\mathbf{i}}_s(t) \tag{29}$$

Under the convergence condition of the IST-NFTSMO, the lumped disturbance is fully compensated by the sliding mode control term. The residual is presented as a zero-mean, approximately normally distributed random signal under normal operating conditions. The validity of this Gaussian assumption has been confirmed by Han et al. [27] for a similar sliding-mode-observer-based fault diagnosis scheme. In their work, the residuals of the improved SMO passed the Kolmogorov-Smirnov test at the 5% significance level and exhibited near-ideal skewness and kurtosis values. Given that the IST-NFTSMO inherits the same observer-residual structure and provides even stronger disturbance rejection, the residual signal in the present system is also expected to follow an approximately normal distribution under healthy conditions. Owing to measurement noise and model parameter perturbations, the residual is not strictly zero. However, its amplitude is confined within a narrow band. Both the mean and standard deviations remained stable.

When an open-circuit fault occurs in the inverter, a half-cycle or full-cycle missing of the actual stator current waveform is observed. The observer still outputs the ideal sinusoidal estimation based on the normalized model. Consequently, a significant deviation between the actual and estimated values was observed. Under these conditions, the statistical properties of the residual signal are significantly altered: the mean shifts from zero to a non-zero value; the standard deviation increases substantially; and the positive-negative sign distribution of the residual becomes asymmetric. These variations are manifested in two dimensions: the amplitude statistics and the sign direction information of the residuals. The former can be employed for sensitive fault detection, whereas the latter can be employed for the precise localization of the faulty phase and switch.

## 4. OPEN-CIRCUIT FAULT DIAGNOSIS METHOD BASED ON ALLR-SCR HYBRID FEATURES

### 4.1. Current Residual Distribution Characteristics Under Open-Circuit Faults

Under ideal conditions, the actual current output of the motor drive system is equal to the estimated current produced by the IST-NFTSMO sliding-mode observer. That is, the current residual is zero. When an open-circuit fault occurs in the upper switch of a certain phase, the positive half-cycle of the output current waveform for that phase tends to approach zero. When

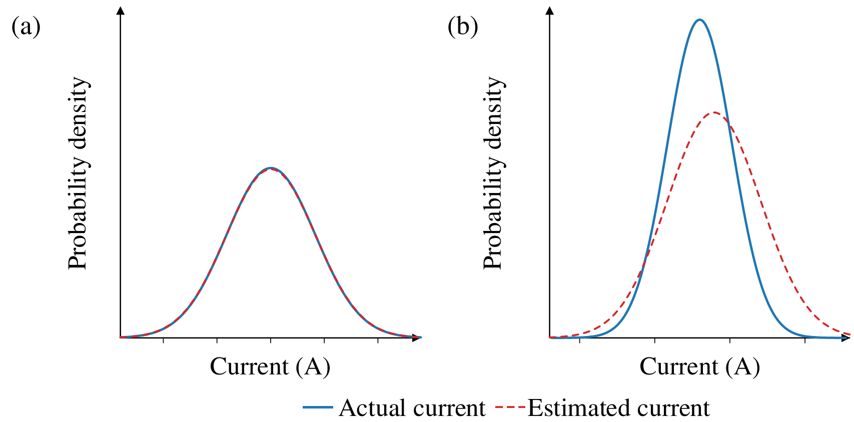


**FIGURE 4**. Probability distribution of current before and after fault.

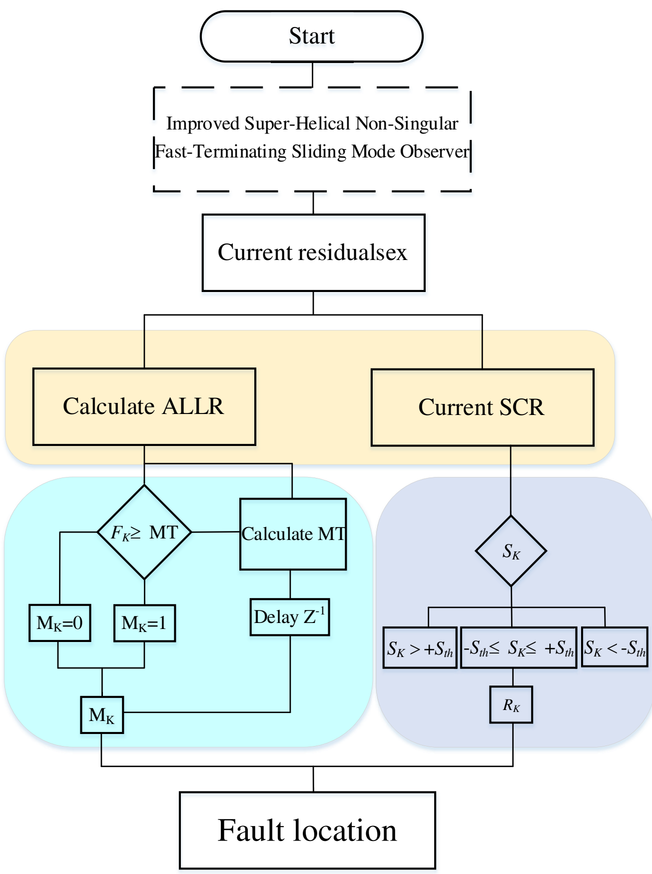


**FIGURE 5**. Principle of fault diagnosis.

an open-circuit fault occurs in the lower switch of a certain phase, the negative half-cycle of the output current waveform for that phase tends to approach zero. The diagnostic principle of the proposed fault diagnosis method is shown in Fig. 5. Fault detection and localization are performed based on the residual between the estimated and actual currents under fault conditions, combined with the fault information contained in the residual.

### 4.2. Statistical Feature Extraction of Current Residual

The probability distributions of the actual and estimated currents before and after the open-circuit fault were examined to evaluate the accuracy and effectiveness of the IST-NFTSMO. The results were presented in Fig. 4, which shows the probability distributions of the actual and estimated currents before and after the open-circuit fault.

As shown in Fig. 4, under normal conditions, both the actual and estimated currents closely followed a normal distribution. Their means and standard deviations were approximately equal. However, after the occurrence of an open-circuit fault, both the actual and estimated currents deviated from the normal distribution. Their means and standard deviations were shifted from those observed under normal conditions.

By exploiting this fault characteristic, the ALLR was developed as a fault feature based on the probability density functions (PDFs) of the actual and estimated currents. The expression is as follows:

$$F_k = \ln\left(\frac{\langle P_k(i_k)\rangle}{\langle \hat{P}_k(i_k)\rangle}\right), \quad k \in \{a, b, c\} \tag{30}$$

In (30), $P_k(i_k)$ and $\hat{P}_k(i_k)$ represent the PDFs of the actual and estimated currents, respectively, and $\langle\cdot\rangle$ denotes the signal cycle-averaged value. The expressions are as follows:

$$P_k(i_k) = \frac{1}{\sigma(i_k)\sqrt{2\pi}} \exp\left(-\frac{(i_k - \mu(i_k))^2}{2\sigma(i_k)^2}\right) \tag{31}$$

$$\langle P_k(i_k)\rangle = \frac{1}{T_s}\int_{t-T_s}^{t} P_k(\tau)d\tau \tag{32}$$

where $\mu$ and $\sigma$ represent the mean and standard deviation of the current signal, respectively, and $T_s$ is the fundamental current period. The calculation of the cycle-averaged PDF improves the accuracy of fault diagnosis, because the interference from non-faulty phase fluctuations during the fault period is suppressed.

Moreover, as demonstrated in [27], the ALLR is inherently robust to moderate non-Gaussian noise and transient disturbances, because it primarily captures the shift in the first two moments (mean and variance) induced by the fault, rather than relying on the exact shape of the noise distribution.

Based on the above, the fault detection flag can be defined as:

$$M_k = \begin{cases} 1, & F_k \geq MT \\ 0, & F_k < MT \end{cases} \tag{33}$$

where $MT$ is the diagnostic threshold for ALLR.

The ALLR indicator can sensitively detect whether an open-circuit fault has occurred in the system. However, the fault location cannot be determined directly using the ALLR alone. To distinguish between faulty upper-arm and lower-arm switches, a statistic that is highly sensitive to the residual direction and computationally simple is required; that is, the signed cumulative ratio (SCR). The SCR is defined as the arithmetic average of the residual signs within a sliding window. For the $k$-th phase with a residual window vector of length $N$, $\mathbf{r}_k = [r_k(1), r_k(2), \ldots, r_k(N)]^T$, the SCR is calculated as:

$$S_k = \frac{1}{N} \sum_{j=1}^{N} \text{sign}(e_k(j)) \tag{34}$$

where sign$(\cdot)$ is the sign function, which takes values of $+1$, 0, or $-1$. The SCR ranges from $-1$ to $+1$. It intuitively reflects the ratio of positive to negative signs within the window: $S_k = 0$ indicates that positive and negative signs are equally distributed; $S_k > 0$ indicates that positive values are dominant; $S_k < 0$ indicates that negative values are dominant.

Under normal operating conditions, the residual fluctuates symmetrically around zero. The probabilities of positive and negative signs are approximately equal, and the SCR approaches zero ($S_a = S_b = S_c \approx 0$). When an upper-arm open-circuit fault occurs (considering phase-A switch S1 as an example), the current path in the positive half-cycle is blocked. The actual current is forcibly clamped to zero or severely attenuated during the positive half-cycle, whereas the estimated current maintains a complete sinusoidal waveform. Consequently, the residual exhibits large negative values during the positive half-cycle. The current in the negative half-cycle was barely affected, and the residual approaches zero. Under this condition, the signs of the vast majority of residual data points within the window are negative, and the SCR becomes significantly negative ($S_a \ll 0, e.g., S_a \leq -0.5$). Similarly, when a lower-arm open-circuit fault occurs (taking phase-A switch T4 as an example), the current in the negative half-cycle is missing. The residual exhibits large positive values during the negative half-cycle, and the SCR becomes significantly positive ($S_a \gg 0$).

By combining the SCR with the preset threshold $\pm S_{th}$, the fault localization variable can be conveniently generated as follows:

$$R_k = \begin{cases} +1, & S_k > +S_{th} \text{ (Upper bridge switch fault)} \\ 0, & -S_{th} \leq S_k \leq +S_{th} \text{ (Normal condition)} \\ -1, & S_k < -S_{th} \text{ (Lower bridge switch fault)} \end{cases} \tag{35}$$

Combined with the fault-phase flag $M_k$ detected by the ALLR, the final fault localization variable is defined as:

$$E_k = M_k R_k \tag{36}$$

The correspondence between its values and the faulty switches is summarized in Table 1.

For cross-side dual-switch open-circuit faults, $M_k = 1$ and non-zero $R_k$ will simultaneously appear in two different phases. The localization algorithm does not immediately terminate the diagnosis upon detection of the first fault. Instead, the ALLR and SCR of the remaining two phases are continuously monitored. If the $S_k$ of the second phase is also detected to exceed the threshold within one fundamental cycle after the first fault is identified, the dual-switch fault type can be directly determined based on the sign combination of $R_k$ in both phases. For single-phase dual-switch open-circuit faults (upper and lower switches open simultaneously), the phase current disappears completely. The residual equals the negative of the estimated current and alternates between positive and negative within one fundamental cycle. Under this condition, the SCR within the window exhibits near-zero periodic oscillation (because the positive and negative signs are nearly equally distributed). However, the ALLR still stably exceeds the threshold. The discrimination condition is as follows: $F_k$ exceeds the threshold, and $S_k$ cannot continuously exceed the threshold in a single direction across multiple consecutive sliding windows, and the SCRs of the other two phases remain normal. Under this condition, the system is determined to have a single-phase dual-switch open-circuit fault, and the localization variable $E_k$ outputs an alternating $[-1, +1]$ sequence for differentiation.

## 4.3. Delayed-Switching Adaptive Threshold Design

### 4.3.1. Statistical Basis and Initialization of ALLR Threshold

Under normal operating conditions, the IST-NFTSMO can accurately estimate the stator currents. The residual approximately follows a zero-mean normal distribution. The ALLR feature is ideally equal to zero. However, due to measurement noise, dead-time effects, and modeling errors, slight fluctuations of $F_k$ still exist during normal operation. To avoid frequent false detections, a reasonable baseline must be determined based on normal historical data. In this study, the absolute values of the three-phase ALLR features are uniformly stored in a sliding queue of length $L$ (the queue length $L$ is typically set to the number of sampling points within one fundamental cycle). The statistical base value of the ALLR threshold is defined as:

$$\varepsilon_F = \text{median}_{\text{upper}}(|F|) + k \cdot \text{IQR}(|F|) \tag{37}$$

where $Q_3(|F|)$ is the upper quartile of the queue, IQR$(|F|)$ is the interquartile range (the difference between the 75th and 25th percentiles), and $\kappa$ is an adjustable coefficient (typical values range from 1.5 to 3). This base value was computed solely from the normal data before the occurrence of a fault. The statistical variation range under normal operating conditions was adequately covered, and the false alarm rate is kept extremely low.

**TABLE 1**. Relationship among fault diagnosis variables, faulty phases, and faulty switches.

| Fault Type | Faulty Switches | $E_a$ | $E_b$ | $E_c$ |
|---|---|---|---|---|
| Cross-side dual-switch open-circuit | $S_1, S_6$ | $+1$ | $-1$ | $0$ |
| | $S_1, S_2$ | $+1$ | $0$ | $-1$ |
| | $S_3, S_4$ | $-1$ | $+1$ | $0$ |
| | $S_3, S_2$ | $0$ | $+1$ | $-1$ |
| | $S_5, S_4$ | $-1$ | $0$ | $+1$ |
| | $S_5, S_6$ | $0$ | $-1$ | $+1$ |
| Same-side dual-switch open-circuit | $S_1, S_3$ | $+1$ | $+1$ | $0$ |
| | $S_1, S_5$ | $+1$ | $0$ | $+1$ |
| | $S_3, S_5$ | $0$ | $+1$ | $+1$ |
| | $S_4, S_6$ | $-1$ | $-1$ | $0$ |
| | $S_4, S_2$ | $-1$ | $0$ | $-1$ |
| | $S_6, S_2$ | $0$ | $-1$ | $-1$ |
| Single-phase dual-switch open-circuit | $S_1, S_4$ | $[+1, -1]$ | $0$ | $0$ |
| | $S_3, S_6$ | $0$ | $[+1, -1]$ | $0$ |
| | $S_5, S_2$ | $0$ | $0$ | $[+1, -1]$ |
| Single-switch fault | $S_1$ | $+1$ | $0$ | $0$ |
| | $S_4$ | $-1$ | $0$ | $0$ |
| | $S_3$ | $0$ | $+1$ | $0$ |
| | $S_6$ | $0$ | $-1$ | $0$ |
| | $S_5$ | $0$ | $0$ | $+1$ |
| | $S_2$ | $0$ | $0$ | $-1$ |

#### *4.3.2. Delayed-Switching Mechanism Integrating Fault States*

However, once a fault occurs, the $F_k$ of the faulty phase increases substantially. If fault data are simply added to the statistical queue, $\varepsilon_F$ will be artificially increased. Consequently, the threshold will lose its sensitivity to subsequent faults. To address this issue, a delayed-switching adaptive threshold concept is proposed, in which a fault-state awareness module is incorporated based on the statistical threshold.

The threshold structure is dynamically adjusted using a delayed signal from the previous control cycle. When no fault is detected in any phase (i.e., $M_a = M_b = M_c = 0$), the diagnostic threshold $MT$ is directly set as the statistical base value plus a small safety margin:

$$MT = \varepsilon_F + \eta \tag{38}$$

When a single-phase fault is detected (e.g., only $M_a = 1$), the threshold is switched to the sum of the average of the ALLR absolute values from the non-faulty phases and the safety margin:

$$MT = \frac{|F_y| + |F_z|}{2} + \eta, \quad y, z \neq x \tag{39}$$

where $\varphi$ represents the two non-faulty phases. Its physical significance lies in the fact that the threshold is determined entirely by the statistical characteristics of the healthy phases. The faulty phase is excluded, and threshold distortion is avoided. If a double-phase fault occurs, the threshold evolves as follows:

$$MT = \frac{5}{6}|F_{\text{non-fault}}| + \eta \tag{40}$$

That is, only the feature of the sole remaining healthy phase is utilized, multiplied by $5/6$ to reduce the risk of an excessively high threshold caused by single-phase fluctuations. When all three phases experience faults (e.g., single-phase dual-switch faults causing abnormal currents in all three phases), the threshold degrades to a fixed minimum value, such that the most basic fault detection capability is maintained.

The above threshold switching is controlled in real time by a delayed fault flag signal. The delay time is only one control cycle, and its impact on the diagnostic speed is negligible. This composite adaptive threshold inherits both the adaptive capability of the statistical threshold for steady-state operating conditions and its low false-alarm rate. Meanwhile, contamination by fault data is prevented by delayed switching. The reliable detection of single-switch and multi-switch faults is achieved.

#### *4.3.3. Setting of SCR Localization Threshold*

The signed cumulative ratio (SCR) is used for fault localization. The normal values fluctuate around zero. By following a similar approach, the distribution of $S_k$ can be statistically characterized under normal operating conditions, and the upper and lower localization thresholds can be set. To simplify the design, a fixed threshold was adopted in this study. When $S_k < -S_{th}$, a lower-arm fault is determined; when $S_k > +S_{th}$, an upper-arm fault is determined. This threshold can be automatically adjusted based on the actual noise level using the median and IQR methods. However, considering that the SCR is insensitive to the amplitude and the sign characteristics are stable, the

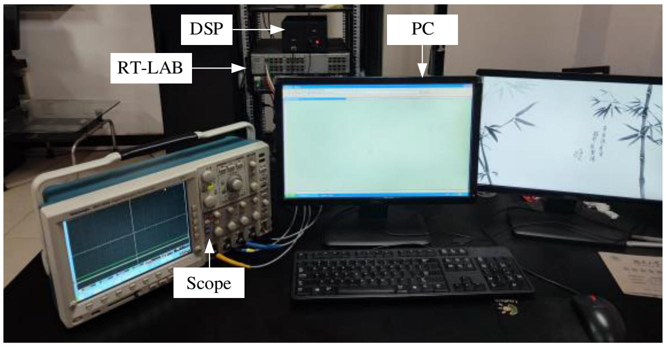


**FIGURE 6**. RT-LAB experimental platform.

fixed threshold already demonstrates good robustness. Therefore, a complex adaptive structure was not introduced.

## 5. EXPERIMENTAL VERIFICATION

### 5.1. RT-LAB Hardware-in-the-Loop Experimental Verification

The RT-LAB experimental platform shown in Fig. 6 was adopted to experimentally validate the proposed open-circuit fault diagnosis method for QZ-source inverters. A TMS320F2812 chip was selected as the digital signal processing (DSP) controller. The core modules of the PMSM system, including the inverter, were constructed using the RT-LAB (OP5600) platform. The data were sampled at a frequency of 10 kHz. The fundamental current period of the PMSM was $T_s = 0.01$ s. The main circuit parameters used in the experiments are listed in Table 2.

The experimental results for the four fault scenarios, that is, cross-side dual-switch open-circuit, same-side dual-switch open-circuit, single-phase dual-switch open-circuit, and single-switch fault, are presented in Figs. 7 and 8. The experimental results are unaffected by the fault sequence and the interval between the faults.

From Fig. 7(a), the diagnostic time for the $S_1$ fault can be quantitatively analyzed. After the fault occurs, $F_a$ rapidly exceeds the threshold $MT$. $M_a$ was set to 1 at approximately 1.6 ms $(16\%T_s)$, completing the fault detection and phase-A localization. Subsequently, within the first complete current half-cycle after $M_a$ was confirmed, $R_a$ exceeded the localization threshold $\pm S_{th}$. Combined with $M_a = +1$ and $R_a = +1$, $E_a = +1$ was output by the system. The faulty switch was ultimately identified as the upper-arm switch $S_1$ of phase A. The total time from fault occurrence to final switch localization was approximately 3.2 ms.

The diagnostic results for the $S_3$ and $S_4$ open-circuit faults are described in Fig. 7(b). After the fault occurs, $F_b$ rapidly increases above $MT$. $M_b$ was set to 1 at approximately 1.6 ms, and the phase-B fault was initially detected. Combined with $M_b = +1$ and $R_b = +1$, the $S_3$ open-circuit fault was confirmed by the system at approximately 1.8 ms. Thereafter, the first switching of $MT$ was executed because of the delayed feedback of $M_b$. During the second fault-dominant phase, $F_a$ exceeds the new threshold $MT$. $M_a$ is set to 1 at approximately 3.4 ms. Combined with $M_a = +1$ and $R_a = -1$, the $S_4$ open-circuit fault is confirmed at approximately 4.4 ms. The second switching of $MT$ ensures that no misdiagnosis occurs during the non-fault-dominant phase. The total time from the occurrence of the first fault to the complete localization of both faults is approximately 4.4 ms (approximately $44\%T_s$).

**TABLE 2**. Circuit parameters.

| Parameters | Values | Unit |
|---|---|---|
| Input voltage ($V_{IN}$) | 150 | V |
| qZS Network Inductor ($L$) | $2 \times 10^{-3}$ | H |
| qZS Network Capacitor ($C$) | $4.7 \times 10^{-4}$ | F |
| Number of pole pairs ($P_n$) | 4 | |
| Switching cycle ($f_s$) | 10 | kHz |
| Stator resistance ($R_s$) | 0.15 | Ω |

The diagnostic results for the $S_1$ and $S_3$ open-circuit faults are described in Fig. 8(a). After the fault occurs, $F_a$ first exceeds the threshold $MT$, and $M_a$ is set to 1 at approximately 1.6 ms. Almost simultaneously, the current residual in phase B also deviates sharply; $F_b$ meets the threshold condition at about 2.0 ms, and $M_b$ is set to 1. Since both $S_1$ and $S_3$ are upper-arm faults, the actual phase currents are blocked during the positive half-cycles, while the estimated currents maintain complete sinusoidal waveforms. Consequently, the residuals $R_a$ and $R_b$ are dominated by large negative values during the fault intervals, causing the signed cumulative ratios $S_a$ and $S_b$ to drop below the negative localization threshold. According to the fault localization rule defined in Table 1, this corresponds to $E_a = +1$ and $E_b = +1$. These two localization variables are successively confirmed at approximately 3.5 ms and 4.0 ms, respectively. The system then identifies that a same-side dual-switch open-circuit fault ($S_1$ and $S_3$) has occurred. The total time from fault occurrence to complete dual-switch localization is approximately 4.0 ms.

The diagnostic results for the single-phase dual-switch open-circuit fault are shown in Fig. 8(b). After the fault occurs, $F_a$ exceeds $MT$ at approximately 1.6 ms, completing the initial detection. Subsequently, because the phase-A current disappears completely, the residual equals the negative of the estimated current. The SCR cannot continuously exceed the threshold in a single direction across multiple consecutive sliding windows. Combined with the ALLR continuously exceeding the threshold, the system determines at approximately 5.4 ms that a single-phase dual-switch open-circuit fault has occurred, and $E_a$ outputs an alternating $[-1, +1]$ sequence. The total time from fault occurrence to fault type confirmation is approximately 5.4 ms.

### 5.2. Comparative Analysis with Existing Methods

To further validate the performance of the proposed method, two typical inverter open-circuit fault diagnosis methods were selected for comparative testing with the proposed method. The comparison results are shown in Fig. 9. In addition, other representative methods from recent years are introduced for multi-dimensional systematic comparison. The comparison results are presented in Table 3.

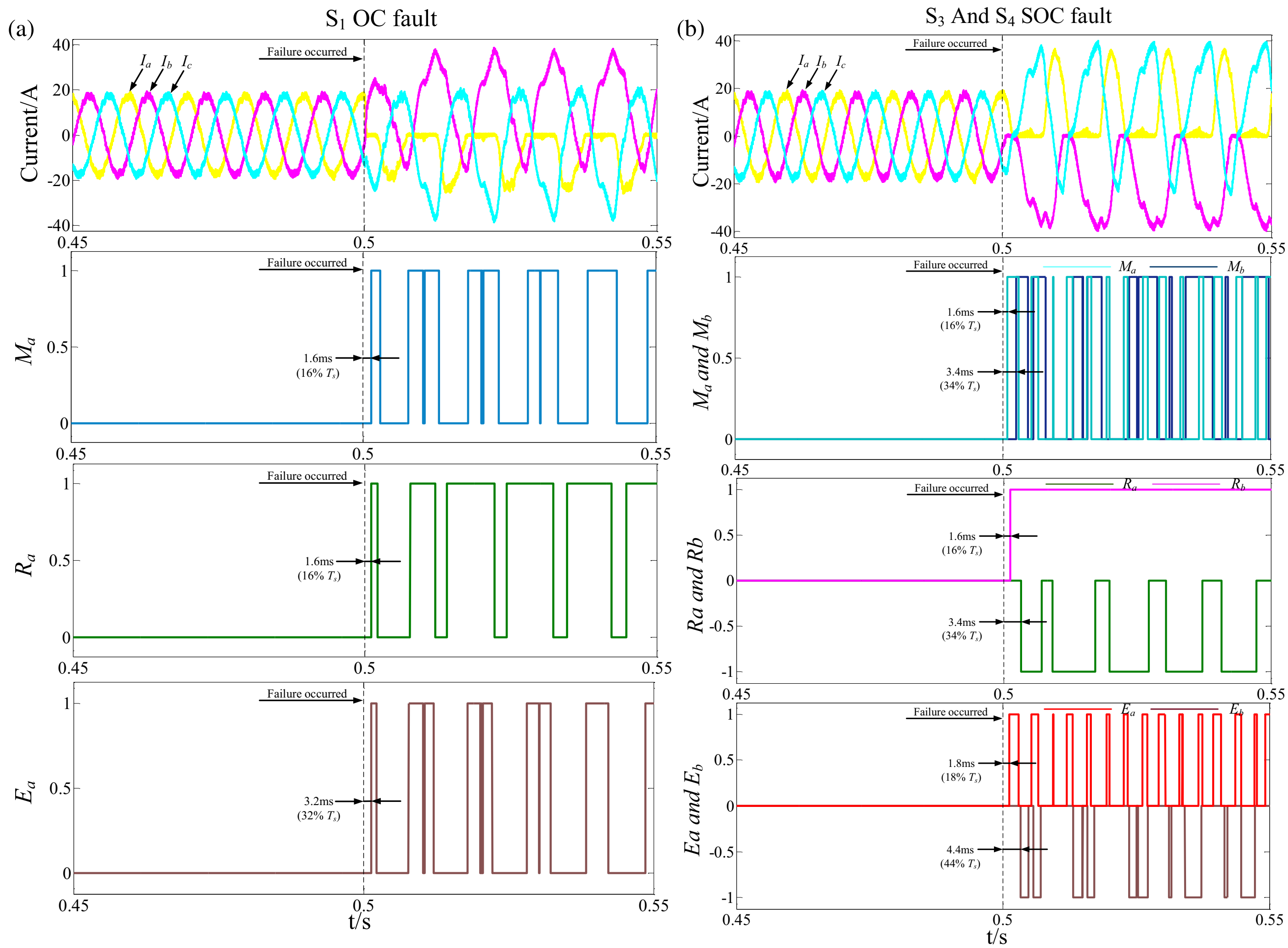


**FIGURE 7**. Fault diagnosis results.

**TABLE 3**. Comparisons among different methods.

| Method | Features | Loads | Additional Hardware | Adaptability | Anti-Interference | Complexity | Speed (%)[1] | |
|---|---|---|---|---|---|---|---|---|
| | | | | | | | Single OC | Dual OC |
| [15] | Voltage-based residual | qZSI | Yes | Medium | Medium | Medium | 25 | – |
| [16] | DNN-based | ZSI | No | High | Medium | High | 18 | – |
| [9] | Average-phase voltage residual | VSI | Yes | Medium | Low | Medium | 15 | 65 |
| [19] | Current-based MPC | PMSM | No | High | Low | Low | 33 | 71 |
| [21] | Current-path based | PMSM | No | High | Medium | Medium | 12 | – |
| Proposed | Current residual & statistical features | qZSI-PMSM | No | High | High | Medium | 32 | 75 |

[1]The diagnostic speed is measured in percentage of the fundamental period (%), taking the average value.

In the direct comparison experiments, the current vector trajectory analysis method proposed in [15] requires the three-phase currents to be transformed into the Concordia coordinate system, and the trajectory slope changes to be analyzed. The computational complexity is moderate in this case. Sensitivity to the current sensor offset was observed. The single-switch fault diagnostic time is $25\%T_s$. The capability for dual-switch fault diagnosis is not provided. The current-path-based rapid diagnosis method proposed in [21] imposes a lower computational burden. The single-switch fault diagnostic time is approximately $12\%T_s$. However, its diagnostic threshold relies on experimental calibration. Both the adaptive capability and

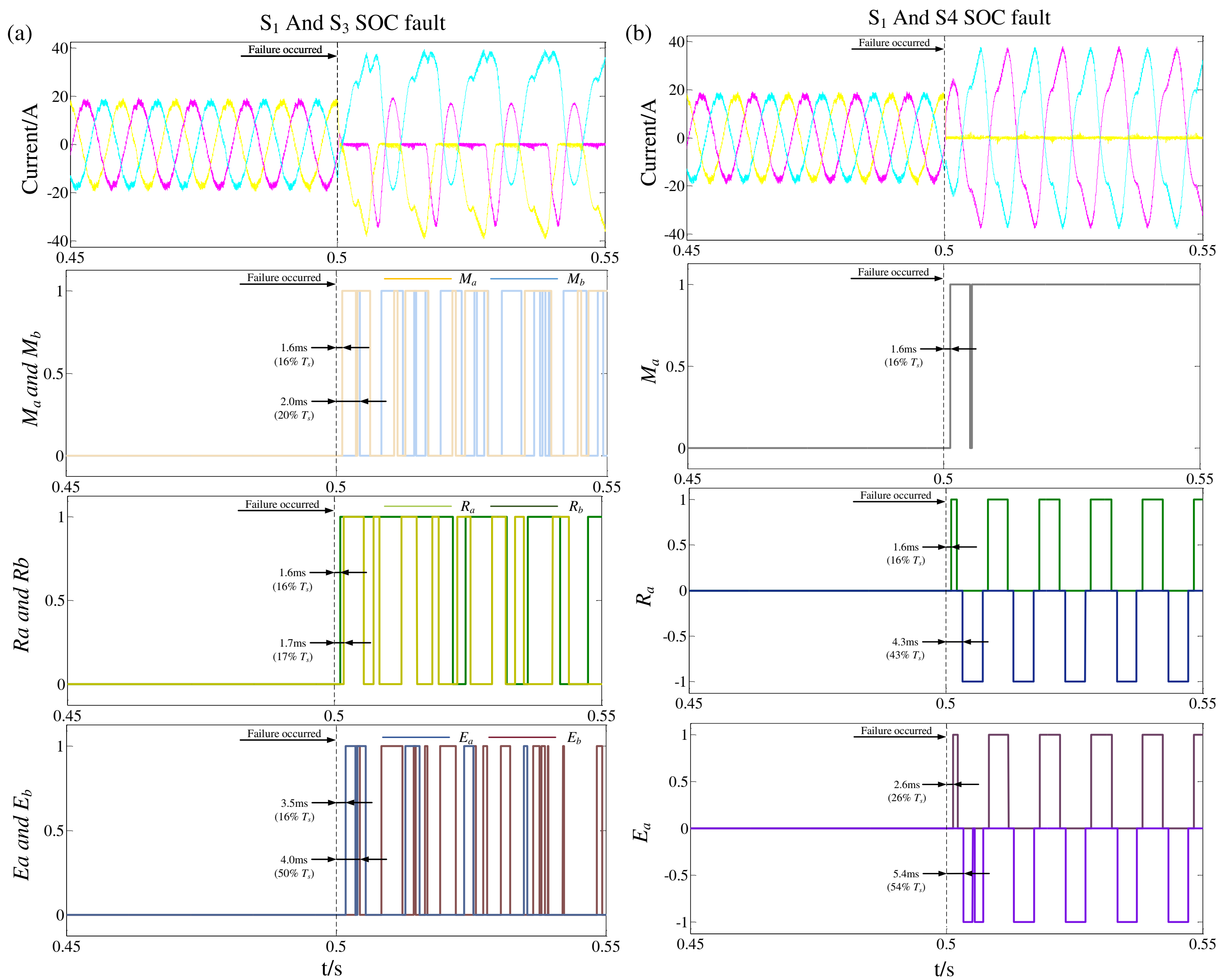


**FIGURE 8**. Fault diagnosis results.

anti-interference performance were at a medium level. In addition, dual-switch fault diagnosis was not addressed.

In the proposed method, the current residual statistical features are generated by the IST-NFTSMO. Rapid fault detection is achieved using ALLR, and precise localization is achieved using SCR. The delayed-switching adaptive threshold mechanism enables an automatic adjustment of the diagnostic threshold according to operating conditions. The experimental results demonstrate that the average time from single-switch fault occurrence to complete switch localization is approximately $32\%T_s$. This speed is slightly slower than the 25% reported in [15] and the 12% reported in [21]. However, the inability of both comparison methods to diagnose dual-switch faults is compensated for by the proposed method. For dual-switch open-circuit faults (including same-side, single-phase, and cross-side dual-switch faults), the average diagnostic time was approximately $75\%T_s$. The reliable localization of all types of dual-switch faults can be achieved within a unified framework.

As can be further observed in Table 3, the voltage-residual-based method in [15] requires additional voltage sensors, resulting in higher hardware expense. Only single-switch faults can be diagnosed using this method. The deep-neural-network-based method in [16] does not require additional hardware. However, its diagnostic reliability is highly dependent on large volumes of training data, and its computational complexity is high. The practical applicability and generalization capability of these models are limited. The voltage residual analysis method in [9] and the current trajectory centroid method in [22] possess dual-switch fault diagnostic capabilities. The diagnostic speeds were comparable to those of the proposed method, with different emphases. However, the former requires voltage sensors and employs fixed thresholds, resulting in limited adaptability. The latter exhibits a lower anti-interference performance under dynamic operating conditions. In summary, the proposed method relies entirely on the system's existing current sensors. No additional hardware is required for this. High adaptive capability and strong anti-interference perfor-

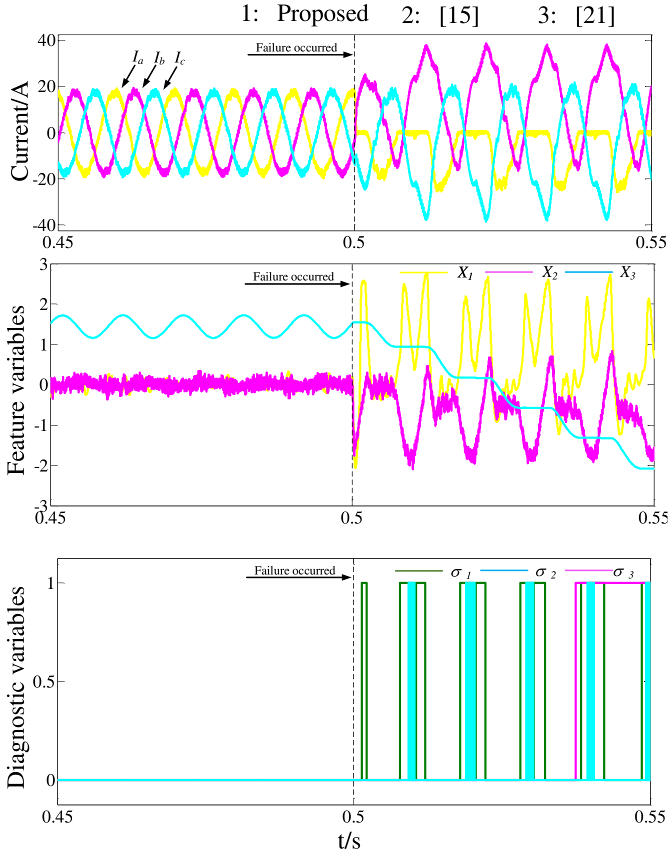


**FIGURE 9**. Comparative analysis of fault characteristics.

mance are achieved using residual statistical features and the delayed-switching adaptive threshold mechanism. Both single-switch and various types of dual-switch open-circuit faults can be covered. A favorable balance was achieved between the diagnostic speed, hardware cost, adaptability, and diagnostic scope.

## 6. CONCLUSION

This paper proposes an open-circuit fault diagnosis method for quasi-Z-source inverter-driven permanent magnet synchronous motor systems based on an improved super-twisting non-singular fast terminal sliding mode observer (IST-NFTSMO) and ALLR-SCR hybrid statistical features. In the proposed method, the current estimation residuals are generated using a sliding-mode observer. Based on the differences in the probability density distributions of the residuals before and after the faults, rapid fault detection is achieved using the average log-likelihood ratio (ALLR). The precise localization of the faulty switch is realized through the signed cumulative ratio (SCR). The designed delayed-switching adaptive threshold mechanism enables an automatic adjustment of the diagnostic threshold according to the operating conditions. Meanwhile, the contamination of the statistical baseline by fault data is effectively prevented.

The proposed method relies entirely on the existing current sensors in the system. No additional hardware or offline training data were required. The diagnosis of single-switch and various types of dual-switch open-circuit faults can be achieved within a unified framework. The experimental results demonstrate that the proposed method can accurately diagnose both single-switch and dual-switch open-circuit faults. The average diagnostic time is approximately $32\%T_s$ for single-switch faults and approximately $75\%T_s$ for dual-switch faults. Furthermore, the proposed method exhibited good robustness against variations in speed and load, sensor noise, and other operating disturbances.

It should be noted that the proposed method only targets open-circuit faults in power switching devices. Short-circuit faults and incipient faults were not addressed. The diagnostic capability under coupled fault scenarios requires further investigation. In the future, the proposed statistical feature framework can be extended to the unified fault diagnosis of multilevel quasi-Z-source inverter topologies.

## ACKNOWLEDGEMENT

This work was supported by the Scientific Research Fund of Hunan Provincial Education Department under Grant Number 24A0395.

## REFERENCES

[1] Hao, Z., Y. Ma, P. Wang, G. Luo, and Y. Chen, "A review of axial-flux permanent-magnet motors: Topological structures, design, optimization and control techniques," *Machines*, Vol. 10, No. 12, 1178, 2022.

[2] Monadi, M., M. Nabipour, F. Akbari-Behbahani, and E. Pouresmaeil, "Speed control techniques for permanent magnet synchronous motors in electric vehicle applications toward sustainable energy mobility: A review," *IEEE Access*, Vol. 12, 119 615–119 632, 2024.

[3] Chen, H., N. A. O. Demerdash, A. M. El-Refaie, Y. Guo, W. Hua, and C. H. T. Lee, "Investigation of a 3D-magnetic flux PMSM with high torque density for electric vehicles," *IEEE Transactions on Energy Conversion*, Vol. 37, No. 2, 1442–1454, 2022.

[4] Gyawali, B., A. M. Ajmal, W. Liu, and Y. Yang, "A review on modulation techniques of Quasi-Z-source inverter for grid-connected photovoltaic systems," *e-Prime — Advances in Electrical Engineering, Electronics and Energy*, Vol. 10, 100809, 2024.

[5] Mande, D., J. P. F. Trovão, M. C. Ta, and T. V. Do, "Dual-source bidirectional quasi-z-source inverter development for off-road electric vehicles," *World Electric Vehicle Journal*, Vol. 13, No. 9, 174, 2022.

[6] Praveena Krishna, P. S., S. Vishnu, A. Dash, V. B. Koreboina, and N. S. Jayalakshmi, "Investigation of bidirectional quasi Z-Source inverter for BLDC drive with modified shoot-through hysteresis current control in low power EV applications," *Cogent Engineering*, Vol. 10, No. 2, 2283279, 2023.

[7] Gannamraju, S. K. and R. Bhimasingu, "Sequential model predictive control of quasi Z-source inverter with fixed frequency operation," *International Transactions on Electrical Energy Systems*, Vol. 31, No. 11, e13068, 2021.

[8] Choi, U.-M., J.-S. Lee, F. Blaabjerg, and K.-B. Lee, "Open-circuit fault diagnosis and fault-tolerant control for a grid-connected NPC inverter," *IEEE Transactions on Power Electronics*, Vol. 31, No. 10, 7234–7247, 2016.

[9] Wang, B., X. Feng, and R. Wang, "Open-circuit fault diagnosis for permanent magnet synchronous motor drives based on voltage residual analysis," *Energies*, Vol. 16, No. 15, 5722, 2023.

[10] Choupan, R., S. Golshannavaz, D. Nazarpour, and M. Barmala, "A new structure for multilevel inverters with fault-tolerant capability against open circuit faults," *Electric Power Systems Research*, Vol. 168, 105–116, 2019.

[11] Mullali Kunnontakath Puthiyapurayil, M. R., M. N. Nasirudeen, Y. A. Saywan, M. W. Ahmad, and H. Malik, "A review of open-circuit switch fault diagnostic methods for neutral point clamped inverter," *Electronics*, Vol. 11, No. 19, 3169, 2022.

[12] Gmati, B., I. Jlassi, S. K. E. Khil, and A. J. M. Cardoso, "Open-switch fault diagnosis in voltage source inverters of PMSM drives using predictive current errors and fuzzy logic approach," *IET Power Electronics*, Vol. 14, No. 6, 1059–1072, 2021.

[13] Yaghoubi, M., J. S. Moghani, N. Noroozi, and M. R. Zolghadri, "IGBT open-circuit fault diagnosis in a quasi-Z-source inverter," *IEEE Transactions on Industrial Electronics*, Vol. 66, No. 4, 2847–2856, 2019.

[14] An, Q., L. Sun, L. Sun, and K. Zhao, "Recent developments of fault diagnosis methods for switclles in three-phase inverters," *Transactions of China Electrotechnical Society*, Vol. 26, No. 4, 135–144, 2011.

[15] Peuget, R., S. Courtine, and J. P. Rognon, "Fault detection and isolation on a PWM inverter by knowledge-based model," *IEEE Transactions on Industry Applications*, Vol. 34, No. 6, 1318–1326, 1998.

[16] Song, B., S. Nie, X. Li, and L. Xu, "Open-circuit fault diagnosis of Z-source inverter via deep neural network," in *2020 Chinese Automation Congress (CAC)*, 7599–7603, Shanghai, China, 2020.

[17] Mendes, A. M. S. and A. J. M. Cardoso, "Voltage source inverter fault diagnosis in variable speed AC drives, by the average current Park's vector approach," in *IEEE International Electric Machines and Drives Conference. IEMDC'99. Proceedings (Cat. No.99EX272)*, 704–706, Seattle, WA, USA, 1999.

[18] Abramik, S., W. Sleszynski, J. Nieznanski, and H. Piquet, "A diagnostic method for on-line fault detection and localization in VSI-fed AC drives," in *10th European Conference on Power Electronics and Applications, EPE'2003*, Toulouse, France, 2003.

[19] Rothenhagen, K. and F. W. Fuchs, "Performance of diagnosis methods for IGBT open circuit faults in voltage source active rectifiers," in *2004 IEEE 35th Annual Power Electronics Specialists Conference (IEEE Cat. No.04CH37551)*, Vol. 6, 4348–4354, Aachen, Germany, 2004.

[20] Sleszynski, W., J. Nieznanski, and A. Cichowski, "Open-transistor fault diagnostics in voltage-source inverters by analyzing the load currents," *IEEE Transactions on Industrial Electronics*, Vol. 56, No. 11, 4681–4688, 2009.

[21] Li, X., S. Li, W. Chen, T. Shi, and C. Xia, "A fast diagnosis strategy for inverter open-circuit faults based on the current path of brushless DC motors," *IEEE Transactions on Power Electronics*, Vol. 38, No. 8, 9311–9316, 2023.

[22] Han, S., Z. Shang, Y. Guo, and X. Jia, "A fault diagnosis method in three-phase voltage inverters based on the normalized current trajectory centroid," *Journal of Electrical Engineering & Technology*, Vol. 19, No. 7, 4421–4434, 2024.

[23] Song, L., M. Liao, R. Wang, and X. Guo, "Open-circuit diagnosis method based on dual-mode voltage residual model for T-type three-level inverter," *Scientific Reports*, Vol. 15, No. 1, 14059, 2025.

[24] Selvakumar, P. and G. Muthukumaran, "A three level npc inverter fault detection and identification using voltage vector residual evaluation based on current path tracking method," *e-Prime — Advances in Electrical Engineering, Electronics and Energy*, Vol. 8, 100541, 2024.

[25] Zhang, G., M. Li, X. Gu, and W. Chen, "Fault diagnosis method for open-circuit faults in NPC three-level inverter based on WKCNN," *CES Transactions on Electrical Machines and Systems*, Vol. 9, No. 2, 234–245, 2025.

[26] Yu, Y. and S. Pei, "Open-circuit fault diagnosis of neutral point clamped three-level inverter based on sparse representation," *IEEE Access*, Vol. 6, 73 499–73 508, 2018.

[27] Han, S., G. Zhao, J. Gao, and J. Jia, "Inverter Open Circuit fault diagnosis method based on ISMO for Improved Efficiency," *Computers and Electrical Engineering*, Vol. 120, 109650, 2024.